Geosci. Model Dev., 19, 11209–11224, 2026
https://doi.org/10.5194/gmd-19-11209-2026
© Author(s) 2026. This work is distributed under
the Creative Commons Attribution 4.0 License.

Geoscientific Model Development
Open Access
EGU

Idealised framework to prescribe sea surface temperatures to investigate the atmospheric circulation response

Fumiaki Ogawa[1,2], **Andrea Marcheggiani**[3,4], **Hisashi Nakamura**[2], **and Thomas Spengler**[3,4]

[1]Faculty of Bioresources, Mie University, Tsu, Japan
[2]Research Center for Advanced Science and Technology, University of Tokyo, Tokyo, Japan
[3]Geophysical Institute, University of Bergen, and Bjerknes Centre for Climate Research, Bergen, Norway
[4]Department of Atmospheric and Cryospheric Sciences, University of Innsbruck, Innsbruck, Austria

Correspondence: Andrea Marcheggiani (andrea.marcheggiani@uib.no)

Received: 28 March 2026 – Discussion started: 10 June 2026
Revised: 9 November 2026 – Accepted: 12 November 2026 – Published: 24 November 2026

Abstract. Midlatitude sea surface temperature (SST) fronts exert a strong influence on storm tracks and westerly jets by modulating lower-tropospheric baroclinicity, moisture availability, and diabatic heating. Yet the sensitivity of the large-scale atmospheric circulation to the detailed structure of these fronts remains difficult to isolate in realistic model configurations. Here we introduce an idealised SST framework for aquaplanet experiments that allows to prescribe the strength, width, and latitude of a midlatitude SST front. The SST profile is constructed from analytically derived meridional gradients, ensuring that changes to the front generate physically consistent moisture distributions through the Clausius–Clapeyron relation.

Using this framework, we conduct a suite of sensitivity experiments to quantify the influence from various aspects in the structure of the SST front on the climatological-mean energy and water cycles as well as the associated atmospheric circulation. Preliminary results demonstrate that increasing the frontal SST gradient or narrowing the frontal width systematically intensifies storm-track activity and strengthens the midlatitude jet, whereas shifting the front meridionally alters the latitudinal position of storm tracks in a nonlinear manner. Warm- and cold-climate experiments further show that imposing a fixed freezing threshold in atmosphere-only setups artificially reduces high-latitude baroclinicity, whereas allowing SSTs to go below freezing produces a more realistic polar thermal structure.

Overall, our results demonstrate that the experimental framework developed in this study provides a useful basis for targeted process studies of how midlatitude SST-front characteristics shape the atmospheric circulation, energy budget, and hydrological cycle.

1 Introduction

The observed link between midlatitude storm tracks, jet streams, and sea surface temperature (SST) fronts underscores the substantial impact of midlatitude SST fronts on the structure and behaviour of the large-scale atmospheric circulation (Nakamura et al., 2004, 2008; Parfitt et al., 2016; Ogawa and Spengler, 2019; Seo et al., 2023). While the SST profile in the tropics and subtropics is essential for the Hadley circulation and subtropical jets (Neale and Hoskins, 2000; Schemm and Röthlisberger, 2024), the frontal SST gradient in the midlatitudes anchors storm tracks through the enhancement of near-surface baroclinicity via turbulent air-sea heat exchanges (Nakamura and Shimpo, 2004; Sampe et al., 2010; Hotta and Nakamura, 2011). Moist diabatic processes further enhance storm-track activity, as the SST front directly modulates moisture availability via the Clausius-Clapeyron relationship (Ogawa and Spengler, 2024). The resulting transient eddy heat and vorticity fluxes maintain the climatological-mean midlatitude jet (Nakamura et al., 2008; Ogawa et al., 2012). Thus, the SST front facilitates the downward transfer of westerly momentum, setting the strength and position of the surface westerlies. However, the extent to which atmospheric circulation depends on the precise spatial structure and intensity of SST fronts remains poorly con-

strained. Hence, we propose a novel framework to configure various aspects of the SST front.

Latent heat fluxes, tied to absolute SST, exert a dominant, *indirect* and positive impact on moist baroclinic development, whereas sensible heat fluxes play a comparatively minor, *direct*, and detrimental role (Haualand and Spengler, 2020; Bui and Spengler, 2021). Moreover, SST fronts shape the distribution of cyclone pathways and precipitation, with enhanced low-level baroclinicity and moisture availability on the warm flank, promoting stronger cyclone intensification and hydrological activity (Tsopouridis et al., 2021b, c). Sharp SST fronts strengthen regional moisture cycling and amplify precipitation–evaporation contrasts within cyclonic and anticyclonic regimes (Okajima et al., 2024). Air–sea heat exchange also contributes to the thermodynamic modulation of individual weather systems, especially within the cold sector, acting predominantly as a local sink of available potential energy (Marcheggiani and Ambaum, 2020). Recent results further emphasise that moist diabatic processes play an active role in restoring baroclinicity and initiating baroclinic development aloft (Marcheggiani and Spengler, 2023), especially within synoptic weather features like cyclones and associated atmospheric fronts (Nonaka et al., 2009; Taguchi et al., 2009; Marcheggiani et al., 2025; Weijenborg and Spengler, 2020), while cold-air outbreaks provide a key pathway for near-surface baroclinicity restoration through intense surface heat fluxes over western boundary current regions like the Gulf Stream and Kuroshio-Oyashio extensions (Marcheggiani and Spengler, 2025).

The large-scale circulation is also highly sensitive to the underlying SST distribution (Brayshaw et al., 2009; Small et al., 2014) with storm tracks and jets being influenced by different aspects of midlatitude SST fronts, notably their strength (Yao et al., 2016), width (Small et al., 2014), and latitude (Ogawa et al., 2012). Maintaining fine-scale SST frontal structures in the Gulf Stream and Kuroshio extension strengthen lower-tropospheric baroclinicity (Taguchi et al., 2009; Brachet et al., 2012; Piazza et al., 2016), enhance cyclogenesis (Booth et al., 2012; Kuwano-Yoshida and Minobe, 2017; Ma et al., 2017; Bui and Spengler, 2021), and shape storm-track and jet behaviour (Small et al., 2014; O'Reilly et al., 2016; Hirata et al., 2016; O'Reilly et al., 2017; Kuwano-Yoshida and Minobe, 2017; Tsopouridis et al., 2021a). Despite this progress, the atmospheric sensitivity to other SST front characteristics, such as frontal width, shape, and latitude, remains comparatively unexplored.

An aquaplanet framework offers a clear advantage over fully coupled simulations to explore the role of SST fronts (e.g., Neale and Hoskins, 2000; Blackburn and Hoskins, 2013). Due to simplified lower-boundary conditions, the setup facilitates a highly controllable experimental setup, making results more comparable across atmospheric general circulation models (AGCMs; Blackburn et al., 2013; Williamson et al., 2013). However, many previous studies either lack midlatitude SST gradients with pronounced frontal strength or rely on fixed SST configurations that are not designed to isolate the effects of the different frontal properties (e.g., Brayshaw et al., 2008; Lu et al., 2010; Brayshaw et al., 2011; Schemm and Röthlisberger, 2024). While the atmospheric response to midlatitude SST fronts has been investigated before (e.g., Sampe et al., 2010; Graff and LaCasce, 2012; Ogawa et al., 2012; Michel and Rivière, 2014; Ogawa et al., 2015, 2016; Bui and Spengler, 2021; Ogawa and Spengler, 2024), the SST setup used in these studies lacks the flexibility to systematically vary multiple frontal characteristics.

Given the need for a more versatile experimental framework to assess how different aspects of SST fronts influence storm-track behaviour, we introduce an idealised SST setup based on the meridional SST gradient that permits independent control of the strength, width, and latitude of a midlatitude SST front. Preliminary results from sensitivity experiments highlight the flexibility of this approach as well as its reliability in generating physically consistent atmospheric responses, allowing us to compare the relative impacts of different properties of the midlatitude SST front as well as the role of absolute SST. While the strength and width of the frontal SST gradient are expected to directly influence the intensity of the midlatitude jet and storm-track activity (Nakamura et al., 2008), the latitude of the SST front is expected to affect their position (Ogawa et al., 2012; Michel and Rivière, 2014). In addition, increasing SST can strengthen storm-track activity and jet intensity through enhanced diabatic heating (Ogawa and Spengler, 2024). Our experimental setup enables a causally-isolated and systematic assessment of their impact, providing a basis for more targeted studies of how different aspects of the SST front influence the atmospheric general circulation, as well as the atmospheric energy and water cycle.

2 Experimental design and methods

2.1 Atmospheric general circulation model

We use the AGCM for the Earth Simulator (AFES) version 4.3 (Ohfuchi et al., 2004; Enomoto et al., 2008; Kuwano-Yoshida et al., 2010). Cumulus convection is represented by the Emanuel mass-flux convection scheme (Emanuel, 1991), radiative transfer follows Nakajima and Tanaka (1986), vertical turbulent diffusion is computed using the Mellor–Yamada scheme (Mellor and Yamada, 1982), and surface turbulent momentum and heat fluxes are calculated using bulk formulae (Louis, 1979; Uno et al., 1995). Our experiments are run with a horizontal resolution of T79 (corresponding to about 1.5° at the Equator), with 56 vertical levels extending to 0.09 hPa. Performing the simulations at higher horizontal resolution up to T239 (0.5° at the Equator) does not qualitatively change our results (see Appendix B).

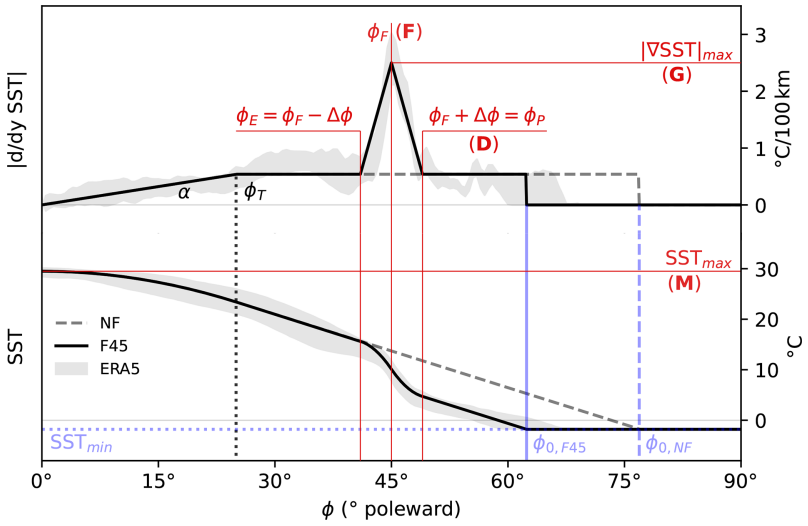


Figure 1. Idealised profiles of meridional SST gradient (above) and corresponding SST (below) for the control experiment (F45), superimposed over ERA5 climatology over the Southern Indian Ocean (MAMSON 1979–2022, 60–80° E). SST gradient increases linearly at rate α until ϕ_T and then stays constant ($\alpha\phi_T$). An SST front is prescribed as a triangular peak in the gradient. The front is centred at ϕ_F (F), has a half-width of $\Delta\phi$ (D), and a set maximum gradient (G). Latitudes $\phi_E = \phi_F - \Delta\phi$ and $\phi_P = \phi_F + \Delta\phi$ represent, respectively, the equatorward and poleward extent of the SST front. The SST profile is obtained by integrating the SST gradient from the equator, where the maximum temperature (M) is set to 29.5 °C. The SST reaches the minimum temperature $SST_{min} = -1.79$ °C at ϕ_0, and is set to constant polewards. Also shown are the profiles for the NF experiment (dashed), where no SST front is prescribed. Red labels (and corresponding capitalised letters) indicate the parameters that are modulated in the different experiments in Figs. 3–7.

2.2 Equinox condition

Our AGCM simulations are run for 66 months, where the first 6 months are counted as a spin-up period and subsequently disregarded. Hence, the effective duration of each simulation is 5 years (60 months). In all simulations, we prescribe equinox conditions with the orbital parameters and solar declination fixed to those of 20 March. Annual mean zonally symmetric ozone concentrations are prescribed to match the climatology from the JRA-3Q Reanalysis (Kosaka et al., 2024) on 20 March, with the average taken over the Northern and Southern Hemispheres to ensure symmetry across the two hemispheres. This symmetry ensures that the climatological mean circulation in the Northern and Southern Hemisphere are effectively identical (not shown), allowing us to average the two hemispheres, thereby doubling the effective data length to 10 years. All our results are thus based on the average of both hemispheres.

2.3 Diagnostics

For efficient comparison of the different simulations, we employ a specific set of diagnostics. Storm-track activity is measured separately in the upper-troposphere by meridional wind variance $[v'v']$ at 300 hPa as a proxy of synoptic-scale eddy kinetic energy and in the lower-troposphere by poleward eddy heat flux $[v'T']$ at 850 hPa, where square brackets denote zonal averaging. Throughout this study, primes denote time anomalies of an 8 d high-pass-filtered component using a Butterworth filter as in Nakamura et al. (2004) to extract transient eddy activity. Differences in the zonal momentum budget are assessed using zonally-averaged climatologies of zonal wind u and the divergence of eddy momentum flux $[u'v']$ at 200 hPa, as in Nakamura et al. (2008). The response of the water cycle is quantified through total precipitation P (convective + large-scale) and evaporation E. The diabatic eddy energy generation (GE) is also examined, as in Ogawa and Spengler (2024, their Eq. 19).

3 Idealised SST profile

In contrast to Nakamura et al. (2008) and Ogawa et al. (2012), we do not base our SST profile on observations from a specific ocean basin to avoid undesired basin-specific fine structures in the SST and its meridional gradient that could obscure the impacts of SST fronts, as noted in Ogawa and Spengler (2024). We therefore analytically prescribe the meridional profile of SST gradients and maximum SST at the Equator, and derive the SST profile by integrating the SST gradient poleward from the Equator (as illustrated in Fig. 1). Our aim is not to exactly replicate observations, but rather to ensure that the imposed SST profile yields a realistic tropospheric circulation.

In prescribing the tropical SSTs, we follow previous aquaplanet experiments (Nakamura et al., 2008; Ogawa et al., 2012) and use the climatological mean SST gradient in the tropical South Indian Ocean, zonally averaged between

Table 1. Experiments using zonally symmetric SST profiles. Control run (F45) is in the top row. The four left columns show the parameters in Eq. (1) that were specified for the individual experiments. For F45, all the parameters are explicitly indicated. For the other individual experiments, parameters that remain unchanged from the F45 case are indicated by an asterisk (*), while those that were modified are highlighted in bold. For the no-front experiment (NF), front-related parameters are omitted. For the F45 ± 5 experiments, the SST profile corresponds to that for F45 with a uniform addition/subtraction of 5 °C.

unit exp. id	$\lvert\nabla\mathrm{SST}\rvert_{\max}$ °C per 100 km G	$\Delta\phi_\mathrm{F}$ ° lat D	ϕ_F ° lat F	$\mathrm{SST}_{\max}$ °C M	$\mathrm{SST}_{\mathrm{mean}}$ °C	$\Delta\mathrm{SST}_{\text{x-front}}$ °C
F45	2.5	4	45	29.5	17.2	10.9
NF	–	–	–	*	18.9	–
G1.5	**1.5**	*	*	*	18.0	7.3
G3.5	**3.5**	*	*	*	16.7	14.5
D2	*	**2**	*	*	18.0	5.5
D6	*	**6**	*	*	16.7	16.4
F35	*	*	**35**	*	16.3	10.9
F55	*	*	**55**	*	18.0	10.9
M24.5	*	*	*	**24.5**	13.0	10.9
M34.5	*	*	*	**34.5**	21.9	10.9
F45−5	*	*	*	**24.5**	12.2	10.9
F45+5	*	*	*	**34.5**	22.2	10.9

60–80° E, for March to May and September to November (MAMSON) from 1979 to 2022 from ERA5 as reference (Hersbach et al., 2020). Mimicking the observed tropical profile, we approximate the SST gradient as linearly increasing from the Equator at a rate $\alpha = 0.0157\,^\circ\mathrm{C}\ (100\,\mathrm{km})^{-2}$ to reach the subtropical edge at latitude $\phi_\mathrm{T} = 25°$ (Fig. 1). We point out that unit conversion from °C $(100\,\mathrm{km})^{-2}$ to °C $(^\circ\,\mathrm{lat})^{-2}$ is required before multiplying α with latitude. The resulting SST profile differs from Ogawa et al. (2012), who prescribed the tropical SST profile as the observed climatology in the South Indian Ocean, leading to spurious effects from the observed subtropical peak in the SST gradient (Ogawa and Spengler, 2024).

Outside the tropics (i.e., polewards of ϕ_T), the SST gradient is held constant at $\beta = \alpha\phi_\mathrm{T}$, corresponding to the value reached at the subtropical edge. We then superimpose a midlatitude SST front, represented as a symmetric triangular peak in the SST gradient profile, where the front is defined by three parameters: its central latitude, ϕ_F; its half-width, $\Delta\phi$; and the maximum gradient reached at its centre, $\lvert\nabla\mathrm{SST}\rvert_{\max}$. Poleward of the front, the gradient reverts to its non-frontal value, β, and remains constant until the freezing latitude, ϕ_0, where the absolute SST reaches the seawater freezing point, set to $\mathrm{SST}_{\min} = -1.79\,^\circ\mathrm{C}$, as in previous studies (Ogawa et al., 2012, 2016). Figure 1 provides a graphical example of the idealised gradient profile described so far.

Analytically, the SST gradient profile is prescribed by

$$\nabla\mathrm{SST}(\varphi) = \operatorname{sgn}\varphi \times \begin{cases} \alpha|\varphi| & |\varphi| \le \phi_\mathrm{T} \\ \beta & \phi_\mathrm{T} < |\varphi| \le \phi_E = \phi_\mathrm{F} - \Delta\phi \\ \beta + \gamma(|\varphi| - \phi_E) & \phi_E < |\varphi| \le \phi_\mathrm{F} \\ \beta - \gamma(|\varphi| - \phi_P) & \phi_\mathrm{F} < |\varphi| \le \phi_P = \phi_\mathrm{F} + \Delta\phi \\ \beta & \phi_P < |\varphi| \le \phi_0 \\ 0 & \phi_0 < |\varphi| \le 90° \end{cases}, \quad (1)$$

where $\gamma = (\lvert\nabla\mathrm{SST}\rvert_{\max} - \beta)/\Delta\phi$ represents the slope of the triangular peak associated with the SST front. The corresponding SST profile is then given by integrating Eq. (1) poleward from the Equator, where we set a maximum temperature $\mathrm{SST}_{\max}$,

$$\mathrm{SST}(\varphi) = \mathrm{SST}_{\max} + \int_{0^\circ}^{\phi} \nabla\mathrm{SST}\,\mathrm{d}\varphi. \quad (2)$$

The full derivation and analytical expression for the SST profile are given in Appendix A.

The idealised SST profile in Eq. (1) allows us to systematically explore the sensitivity of the AGCM response to various aspects of midlatitude SST fronts. Specifically, we modulate the maximum gradient of the SST front (G experiments), its latitudinal width (D experiments), and its latitudinal position (F experiments), to consider stronger (G3.5) and weaker

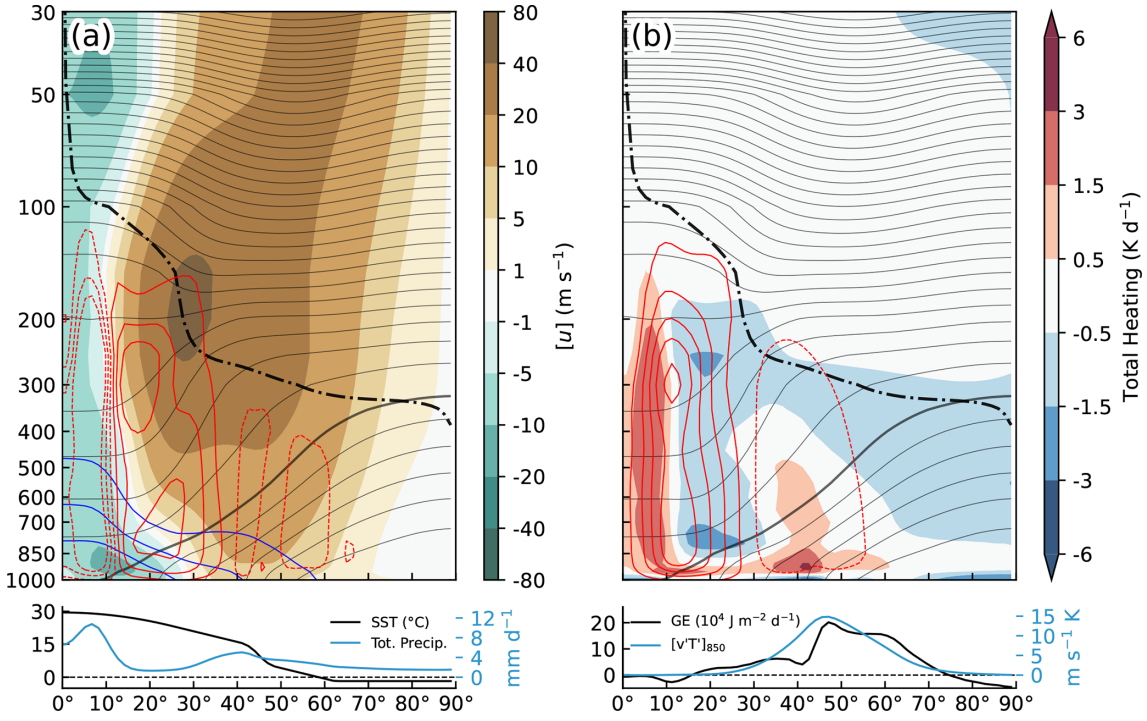


Figure 2. Climatological zonal profiles based on the control experiment F45. **(a)** Zonal wind u (shading), potential temperature (black contours, every 5 K below 300 K, every 10 K above; thick contour marks 300 K), vertical pressure velocity (red contours, ±0.2, ±0.6, and ±1.0 hPa h^{-1}, negative dashed), specific humidity (blue contours, 3, 7, and 11 g kg^{-1}), dynamic tropopause level (dash-dotted line, 2 PVU); below, SST profile (black) and total precipitation (blue). **(b)** Total diabatic heating (shading), Eulerian mean streamfunction (red contours, every 4×10^{10} kg s^{-1} between $\pm 30 \times 10^{10}$ kg s^{-1}), potential temperature (as in **a**), dynamic tropopause level (as in **a**); below, GE term (black) and $[v'T']$ at 850 hPa (blue).

(G1.5) fronts, wider (D6) and narrower (D2) fronts, and poleward (F55) and equatorward (F35) fronts, respectively.

Additionally, we adopt two approaches to changing absolute SST by varying the maximum SST at the Equator. In the first, the freezing temperature is held fixed to realise the ice-free ocean (M experiments), while in the second, a uniform change in SST is applied across all latitudes (F45 ± 5 experiments), allowing SSTs to fall below freezing in the cold-climate experiment (F45–5). This implies that, in F45 ± 5, SST gradients do not necessarily follow Eq. (1) at polar latitudes. Despite below-freezing SSTs at polar latitudes in F45–5, the results remain physically meaningful, as observed polar surface temperatures commonly go well below freezing over sea ice. Summer and winter conditions can be obtained by introducing a meridional shift in the SST gradient profile in Eq. (1), though we do not consider this configuration in this study.

For both the G and D experiments, the no-front configuration (NF) without a midlatitude frontal SST gradient allows us to examine the impact of introducing (or strengthening) an SST front. In the F experiments, comparing shifted fronts with the NF configuration further highlights the impact of the presence of the SST front.

We define a control experiment in which the SST front is centred at $\phi_F = 45°$ (F45) with a maximum gradient of 2.5 °C per 100 km (G2.5) and a half-width of $\Delta\phi_F = 4°$ (D4) in latitude (so 8° in total width), and the maximum temperature at the Equator is set to 29.5 °C. For simplicity, we refer to the control experiment as F45. The SST front in F45 is characterised by a cross-frontal temperature difference, $\Delta SST_{x\text{-front}}$, of 10.9 °C, while the global mean SST corresponding to this SST profile is 17.2 °C. We then conduct a series of experiments where we vary only one parameter at a time. The configurations for all our experiments, as well as corresponding $\Delta SST_{x\text{-front}}$ and global mean SST, are summarised in Table 1. For comparison, the front prescribed in Nakamura et al. (2008) is also centred at 45°, has a maximum gradient of 1.8 °C per 100 km, and a total latitudinal width of 13°.

4 Results

In order to identify the response of the atmospheric circulation to different SST frontal characteristics, we modify the different frontal parameters (G, D, F, M) and modulate them one at a time. In the following subsections, we focus on the

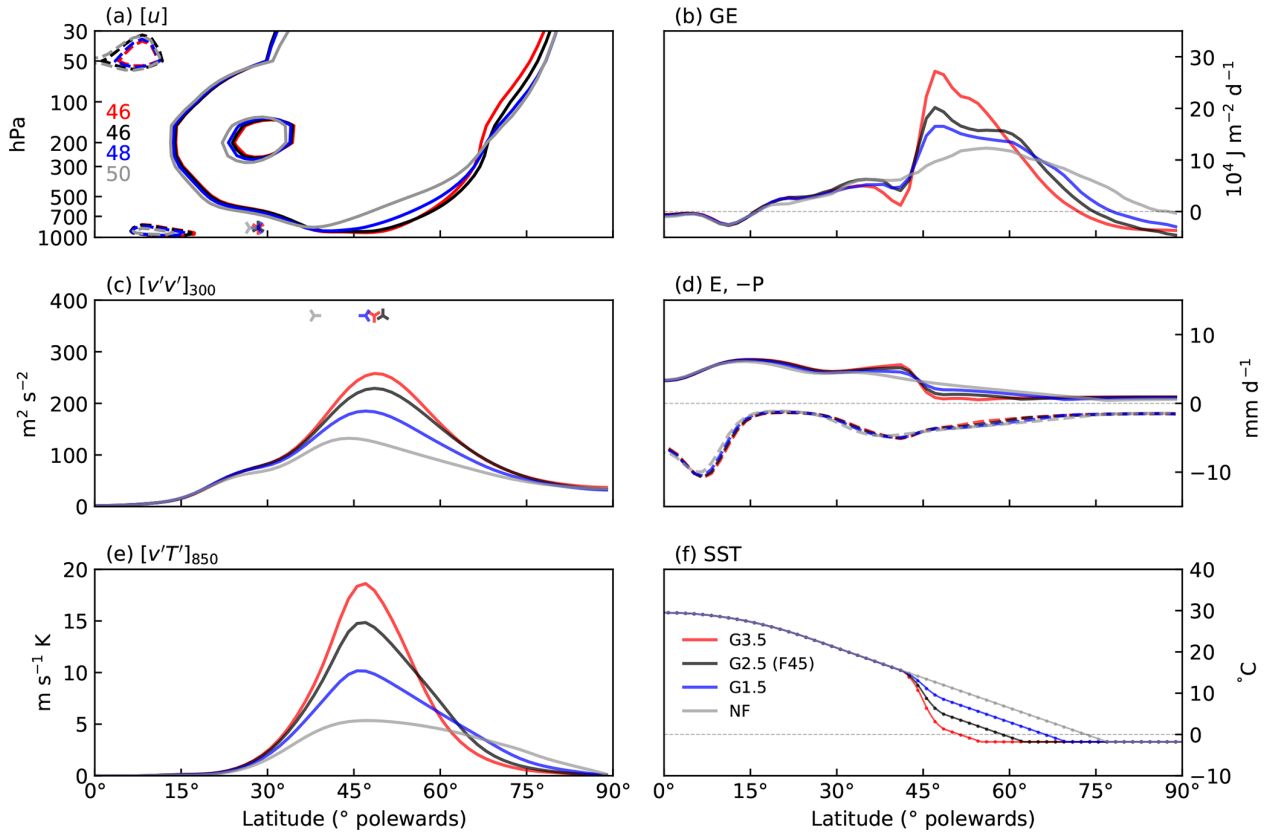


Figure 3. Climatological zonal means based on G3.5 (red), G2.5 (corresponding to F45; black), G1.5 (blue), and NF (grey). **(a)** Zonal wind $[u]$ (contours at -10, 10, 40 m s^{-1}, negative dashed), with maximum value within subtropical jet noted accordingly; markers indicate the latitude of reversal of surface $[u]$ (specific orientation bears no meaning). **(b)** GE term. **(c)** $[v'v']$ at 200 hPa; markers indicate the latitude of maximum momentum flux divergence at 200 hPa. **(d)** Zonally-averaged evaporation (E, solid) and precipitation (P, dashed, multiplied by -1). **(e)** $[v'T']$ at 850 hPa. **(f)** SST profile as represented in the model at T79 resolution (dots) and its analytical form (solid lines).

response to each parameter individually compared to the control experiment presented in the previous section.

4.1 Control (F45)

The climatological zonal wind field reveals two clearly separated jets (Fig. 2a). The subtropical jet is centred near 30° with its core located at around 200 hPa, where westerly wind speed reaches approximately 45 m s^{-1}. Below the core, the wind speed drops to almost zero at the surface, corresponding to the axis of the subtropical high-pressure belt (Nakamura et al., 2004). In contrast, the midlatitude jet has a deeper vertical structure that extends down to the surface, characteristic of an eddy-driven jet (Nakamura et al., 2004), with maximum surface westerlies occurring between 40 and 50°, collocated with the SST front (bottom of Fig. 2a).

The Hadley cell spans from the Equator to about 25–30°, aligning with the latitude of the subtropical jet (Fig. 2b). Poleward of the Hadley cell, the Ferrel cell extends towards 50–55°. The dynamical tropopause, identified by the 2-PVU contour (Bluestein, 1993; 1 PVU $= 10^{-6}$ m^2 s^{-1} K kg), drops sharply across the subtropical jet, consistent with the transition from the tropical warm convection zone into the midlatitude baroclinic zone. These large-scale circulation features indicate that the control simulation produces a reasonable basic-state climatology of the zonally averaged tropospheric circulation.

The moisture distribution is tightly linked to the SST profile, with specific humidity being highest in the warm subtropics and decreasing abruptly across the SST front (blue contours in Fig. 2a). Simulated climatological-mean total precipitation is also characterised by a reasonable meridional structure, reaching its absolute maximum of about 25 mm d^{-1} between 5 and 10° (bottom of Fig. 2a) in correspondence with the strongest vertical motion (Fig. 2a) associated with the ascending branch of the Hadley cell (red contours in Fig. 2b).

A secondary precipitation maximum occurs around 40°, on the equatorward flank of the midlatitude SST front (bottom of Fig. 2a). This peak is associated with enhanced midlatitude cyclone activity, evident in the maximum of poleward eddy heat transport $[v'T']$ at 850 hPa (bottom of Fig. 2b) and the prominent baroclinic structure of the lower-

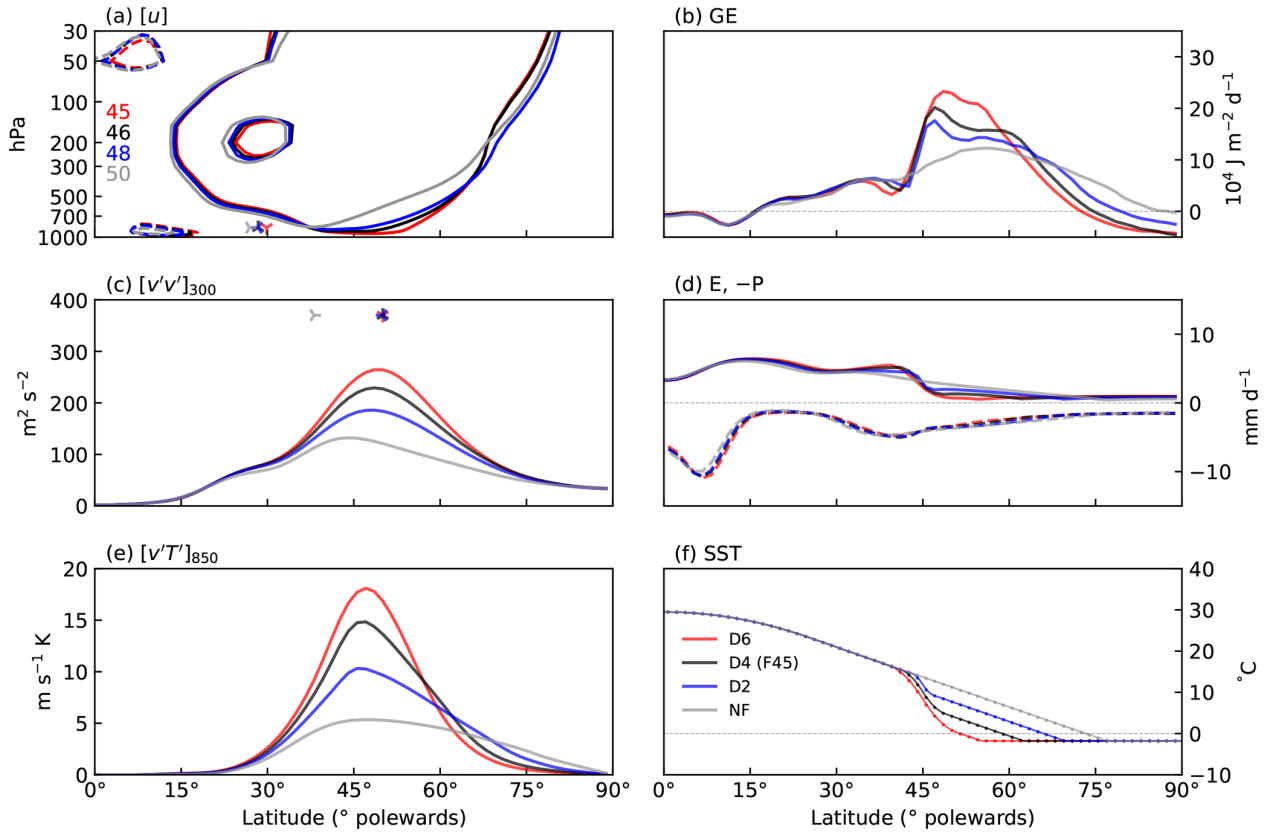


Figure 4. As in Fig. 3, but for D6 (red), D4 (corresponding to F45; black), D2 (blue), and NF (grey).

tropospheric isentropic surfaces (black contours in Fig. 2a–b).

Both precipitation maxima correspond to regions of strong diabatic heating (Fig. 2b), confirming that latent heating dominates the total diabatic budget (Hotta and Nakamura, 2011; Papritz and Spengler, 2015). Whereas total heating peaks slightly equatorward at around 40–42°, diabatic generation of eddy available potential energy (GE) is strongest on the poleward side of the SST front. The aforementioned overall characteristics are consistent with previous aquaplanet simulations using similar idealised SST profiles (e.g., Ogawa and Spengler, 2024; Schemm and Röthlisberger, 2024), indicating that the simplified SST profile given in Eq. (1) provides a suitable basic state in terms of both the general circulation and hydrological cycle.

4.2 Sensitivity to maximum gradient (G)

The largest differences in zonally-averaged, climatological-mean zonal wind $[u]$ are found in the lower troposphere, where the separation between the subtropical and the mid-latitude jet is more pronounced in both the control and G3.5 experiments compared to G1.5 and NF (Fig. 3a). The sensitivity is largest at and poleward of the SST front, while no marked differences are found equatorward of the front. The latitudes of the zonal wind reversal at the surface (i.e., the subtropical high-pressure belt) are also insensitive (markers in Fig. 3a).

In the upper troposphere, the differences in $[u]$ among the experiments are also marginal, although the maximum wind speed in the subtropical jet core is slightly stronger in G1.5 and NF (50 m s^{-1}) compared to the control and G3.5. This is most likely due to the midlatitude jet being more often merged with the subtropical jet in G1.5 and NF.

In terms of storm-track activity, the maximum amplitude of both $[v'v']$ (Fig. 3c) and $[v'T']$ (Fig. 3e) scale with G, suggesting that the maximum gradient of the SST front exerts a direct influence on the intensity of storm-track activity both near the surface and in the upper troposphere. The storm tracks' latitude, however, seems rather insensitive to the frontal intensity.

The latitude of maximum momentum convergence (markers in Fig. 3c) is also overall unaffected, though there is a clear equatorward shift for the NF experiment. It is important to note, however, that for larger values of G, the prescribed SST profiles reach the freezing temperature at much lower latitudes than in the weaker-G and NF experiments. This results in extensive regions poleward of the freezing latitude (ϕ_0) with no meridional SST gradients, suppressing temperature advection and consequently a weakening of $[v'T']$. As

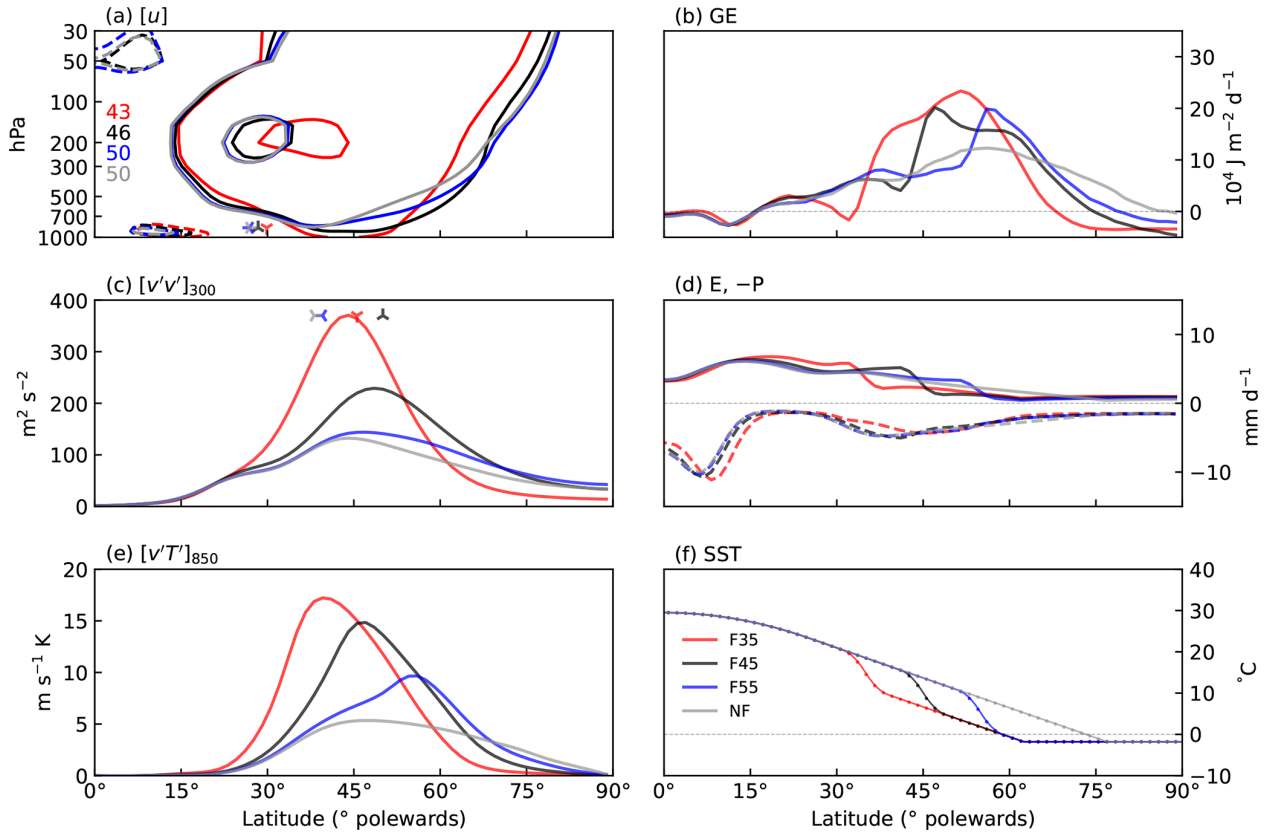


Figure 5. As in Fig. 3, but here for F35 (red), F45 (black), F55 (blue), and NF (grey).

a consequence, eddy heat transport diminishes noticeably poleward of ϕ_0 in the strong-G experiments (Fig. 3e).

The diabatic generation term (GE) responds to changes in the maximum SST gradient mainly poleward of the SST front, where GE reaches its largest values in the G3.5 experiment (Fig. 3b). In the weaker-G experiments, a secondary GE peak develops farther poleward around 50°. This secondary peak becomes the dominant peak for NF, maximising between 50 and 60° and suggesting the presence of a preferred latitude for diabatic generation even in the absence of a midlatitude SST front.

4.3 Sensitivity to frontal width (D)

The zonal jet response is qualitatively similar to the G-experiments (Fig. 4a). While changes remain rather subtle across the different D-experiments, the midlatitude jet extends slightly farther poleward at the surface in the D6 experiment and the subtropical jet is weakest at 45 m s^{-1}. The latitude of maximum momentum convergence (Fig. 4c) is virtually unchanged from the control (D4) at around 48°. The latitude of maximum storm-track activity, both in terms of upper-tropospheric kinetic energy ($[v'v']$, Fig. 4c) and lower tropospheric meridional heat transport ($[v'T']$, Fig. 4e), is also rather insensitive to changes in D, although there is a slight poleward shift for experiments with wider fronts, similar to what is observed in the G-experiments. Again, this might be due to the larger extent of polar SSTs at the freezing temperature in D6 compared to control and D2, which negatively affects $[v'T']$.

Total precipitation is not visibly affected by changes in the width of the SST front, while extreme suppression of evaporation under the cooler SST condition extends over a wider latitudinal band as the front's width is increased. Between the G- and D-experiments, the corresponding latitudinal profiles of evaporation and total precipitation are overall similar (Figs. 3d, 4d). The corresponding subtle changes in the water cycle, however, result in a weaker enhancement of the primary peak of GE as well as a weaker decrease equatorward of the SST front in D6 than in G3.5 (Figs. 3b, 4b). The GE term almost vanishes around 42° in the G3.5 experiment (Fig. 3b), in contrast with a less marked minimum in D6 (Fig. 4b).

The overall similarity between the D and G experiments might be ascribed to the close resemblance of the corresponding SST profiles (compare Figs. 3f and 4f). Introducing additional experiments with wider and stronger SST fronts (e.g., D8 or G4.5) would provide further insight into the specific role of these two frontal parameters. However, such an investigation is beyond the scope of this study, as the main aim is to showcase the feasibility of using such an idealised

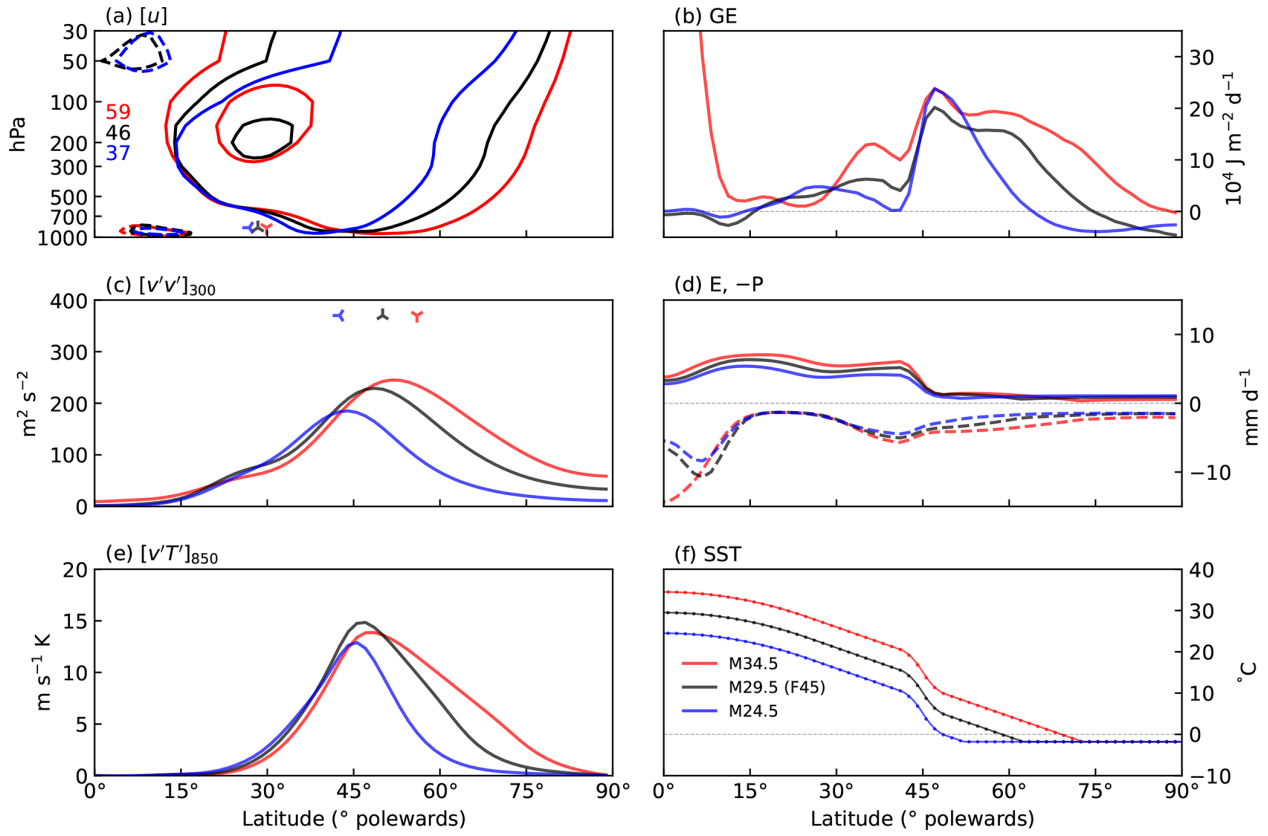


Figure 6. As in Fig. 3, but here for M34.5 (red), M29.5 (corresponding to F45; black), and M24.5 (blue).

SST profile that can be easily modified to test a wider range of scenarios.

4.4 Sensitivity to front latitude (F)

The separation between the subtropical and midlatitude jet is clearest when the SST front is located at higher latitudes (Fig. 5a). The subtropical jet in F45 and F55, and also in NF, is located around 25–30°, with maximum speeds of 46–50 m s^{-1}. The subtropical jet in F35, by contrast, is weaker and shifted poleward, with a maximum speed of 43 m s^{-1} around 35°, suggesting that the subtropical and midlatitude jets in F35 are often merged.

While the midlatitude jet extends to higher latitudes in F45, F55, and NF, it is visibly weaker at the surface than in F35. In fact, surface westerlies are strongest in excess of 10 m s^{-1} in F35 associated with the most enhanced $[v'T']$ in the lower troposphere (Fig. 5e). The latitude of the reversal of surface zonal winds (i.e., subtropical high-pressure belt) shifts equatorward as the SST front is moved polewards, though the shift is rather small (up to 3°).

The anchoring effect of storm-track latitude by the SST front is clearly evident in the lower troposphere. The meridional eddy heat fluxes at 850 hPa show an alignment of the latitude with the SST front (Fig. 5e), confirming the findings by Ogawa et al. (2012). The peak intensity is strongest for F35 and decreases for F45 and F55. A secondary peak hinted at around 45° in F55 is close to the main peak in the NF experiment.

A similarity in storm-track activity between F55 and NF is also evident in the upper troposphere when looking at $[v'v']$ (Fig. 5c). The relationship between the latitude of the SST front and $[v'v']$ is somewhat more complex, as its peak does not clearly shift poleward with the front, but actually retracts equatorward in F55, close to that in NF. A similar sensitivity is also found for the maximum eddy momentum divergence (markers in Fig. 5c).

Consistent with Ogawa et al. (2012), both storm-track activity metrics and the midlatitude jet feature a common enhancement around 40–45°, where they peak even in the absence of an SST front in NF (Fig. 5c, e). The insensitivity of the mean jet latitude to shifts in the SST front likely reflects the fact that the climatological mean jet in the presence of an SST front represents the average of two distinct regimes associated with annular-mode variability (Ogawa et al., 2016). In one regime, the SST front strongly anchors the jet position, whereas in the other, the jet position is governed primarily by internal atmospheric processes, similar to the environment without an SST front (NF). The fact that the mean jet latitude in the F experiments is nearly identical to that in

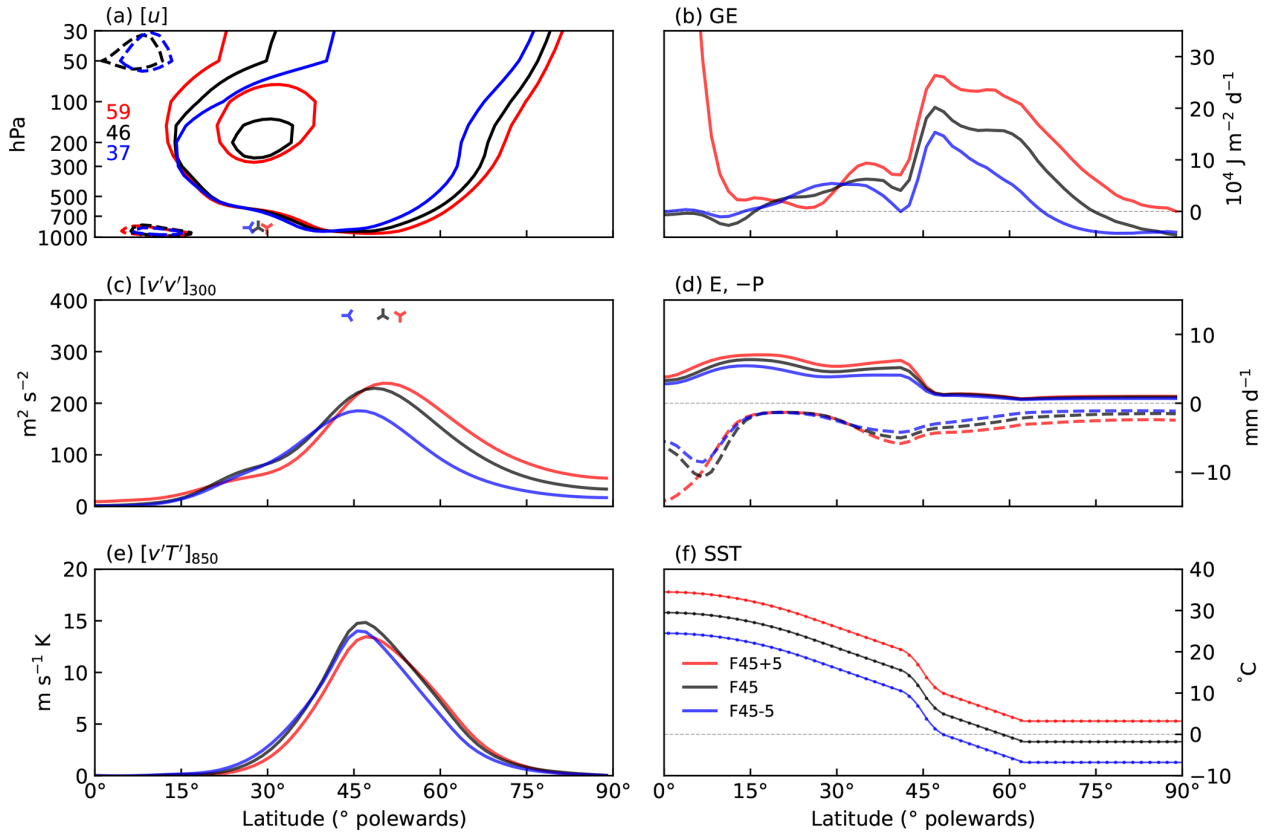


Figure 7. As in Fig. 3, but here for F45+5 (red), F45 (black), and F45–5 (blue).

the NF experiment suggests that the latter regime is strongly reflected in the climatological mean state.

There is a correspondence between the latitude of the SST front and enhanced diabatic generation (GE), consistent with the results by Ogawa and Spengler (2024). However, when the front is closest to the Equator (F35), the peak of GE is located around 50° and not along the SST front. The location of the maximum in F35 is actually close to the location of the highest GE found in the NF experiment, which might also be related to the regime-like behaviour between the two states governed by the SST front and atmospheric internal variability as discussed above (Ogawa et al., 2016).

Total precipitation (Fig. 5d) is not particularly affected by the latitude of the SST front, though we notice a minor poleward shift in the tropical peak and a weakening in the midlatitudes in F35 compared to the other experiments. Evaporation, in contrast, is clearly aligned with the position of the SST front, featuring the typical poleward drop across the SST front.

4.5 Sensitivity to maximum temperature (M)

The subtropical jet is stronger in the warm climate experiments (M34.5 and F45+5) compared to the control and cold climate experiments (M24.5 and F45–5), with maximum mean wind speeds reaching up to 59 m s^{-1} in the former compared to 37 m s^{-1} in the latter (Figs. 6a, 7a). The altitude of the subtropical jet core is nearly proportional to the global mean temperature, which is associated with stronger and thus deeper tropical convection, as evident in the increased total precipitation in the tropics (Figs. 6d, 7d) and the corresponding intensification of the Hadley cell (not shown). The midlatitude jet strengthens and extends poleward across the SST front in the warm climate experiments (M34.5, F45+5), while it is strongest on the equatorward flank of the SST front in the cold climate experiments (M24.5, F45–5).

In the warm climate experiments (M34.5, F45+5), precipitation and GE exhibit a distinct transition toward a single-ITCZ regime, reflected in a pronounced precipitation maximum at the Equator (Figs. 6d, 7d) accompanied by a strong peak in GE collocated with the most vigorous equatorial ascent (not shown). The latitude of the surface westerly-wind reversal shifts slightly poleward in the warmer climate, indicating a modest expansion of the tropical circulation, consistent with climate model simulations (Grise and Davis, 2020), although the subtropical jet itself does not shift appreciably (Figs. 6a, 7a).

Both evaporation and total precipitation largely scale with the mean SST on the equatorward flank of the SST front, consistent with the thermodynamic arguments by Ogawa

and Spengler (2024). With higher SST, precipitation also increases around and poleward of the midlatitude SST front, while evaporation remains almost unchanged poleward of the front (Figs. 6d, 7d). This tendency indicates enhanced poleward eddy moisture transport, consistent with stronger and poleward-shifted storm-track activity (Figs. 6e, 7e) and GE increase in the extra-tropics (Figs. 6b, 7b). Thus, changes in global-mean SST not only modulate the tropical hydrological cycle but also influence the extra-tropical precipitation and diabatic energy generation via modulated eddy activity, with a smaller impact on evaporation.

In the warm climate experiments (M34.5, F45+5), eddy meridional wind variance $[v'v']$ is substantially larger and extends farther poleward than in the cold climate experiments (M24.5, F45–5); the latitude of maximum eddy momentum convergence also shifts poleward with increasing equatorial SST (Figs. 6c, 7c). However, no such tendencies are evident in the meridional eddy heat transport, whose behaviour around and poleward of the SST front is sensitive to whether the freezing temperature in SST is fixed or not (Figs. 6e, 7e), as discussed below.

When the freezing temperature for SST is held fixed (M24.5, M34.5), the warm climate experiment (M34.5) shows enhanced poleward heat transport at subpolar latitudes (Fig. 6e). In contrast, when SSTs are allowed to fall below freezing ($F45 \pm 5$), this increase in heat transport nearly disappears (Fig. 7e) and the corresponding changes in the eddy meridional wind variance are also much smaller (Fig. 7c). Consistently, the midlatitude eddy-driven jet does not extend as far poleward in F45+5 as it does in M34.5 (Figs. 6a, 7a). Together, these results indicate that the strong dynamical responses in the M experiments primarily reflect changes in the total Equator-to-pole temperature contrast rather than changes in global mean SST.

Imposing a fixed freezing threshold in an aquaplanet atmosphere-only model artificially forces warmer surface temperatures in regions where sea ice would otherwise have temperatures far below freezing. The latitudinal shift of the freezing edge in the M24.5–34.5 experiments evidently affects GE (Fig. 6b). While GE in both M24.5–34.5 and $F45 \pm 5$ experiments essentially scales linearly with global mean SST, GE in M24.5–34.5 shows a more complex meridional structure than in $F45 \pm 5$ (Fig. 7b). This suggests that imposing a fixed freezing temperature in aquaplanet experiments with prescribed SST in an atmosphere-only configuration may introduce undesirable constraints on the simulated climate.

Such constraints are not necessarily physical, as maintaining SSTs near the freezing point in the polar regions is no more realistic than allowing them to fall to $-30\,^{\circ}\mathrm{C}/-40\,^{\circ}\mathrm{C}$, which better reflects typical surface temperatures of polar regions covered with sea ice. A more physically consistent treatment would arguably involve prescribing sea ice and associated parameterised surface heat exchanges when specifying very low SSTs far below the freezing point of seawater.

5 Conclusions

We introduced an idealised SST framework for zonally symmetric SST profiles derived directly from their meridional gradients, which are prescribed piecewise using a small set of physically interpretable parameters before integrating polewards from the Equator. Midlatitude SST fronts are introduced as triangular peaks in the imposed SST gradient profile, allowing their strength, width, and latitude to be varied independently. Through the Clausius–Clapeyron relation, changes in the imposed SST profile naturally translate into a different moisture distribution. This experimental setup therefore allows to quantify how the atmospheric circulation, energy cycle, and water cycle respond to variations in key frontal parameters like the maximum gradient (G), frontal width (D), and latitude (F). Tropical SSTs are also technically flexible in this SST design, but are generally left unchanged not to perturb the tropical circulation, especially the Hadley cell, which can directly affect the subtropical jet. We, however, modified the maximum SSTs at the Equator (M) to reveal the response of the atmospheric circulation to uniform warming or cooling.

Variations in the maximum SST gradient and the meridional width of the front exert a direct and systematic influence on storm-track intensity and meridional extent (Figs. 3, 4). These sensitivities emerge robustly across our explored parameter space (G1.5–3.5, D2–6). Preliminary tests (not shown) suggest that extending the range of parameter perturbations (e.g., G4.5, D8) could further clarify the relative roles of gradient strength and frontal width in setting the structure of baroclinic eddy activity.

The relationship between the latitude of the SST front and storm-track behaviour is found to be more complex. While storm-track activity, especially in the lower troposphere, generally migrates with the SST front, its intensity varies nonlinearly. The intensification of baroclinic eddies is most pronounced when the SST front lies close to a dynamically preferred latitude of maximum storm-track activity (Fig. 5c), indicating that the atmospheric response is shaped both by the imposed surface forcing and by the latitude at which baroclinic eddies naturally tend to develop most vigorously.

The warm climate experiments (M24.5–34.5, $F45 \pm 5$) underscore the importance of prescribing adequate SST at polar latitudes. When SSTs are artificially constrained to remain near freezing poleward of a prescribed latitude, this constraint can unintentionally affect baroclinic eddy activity at subpolar latitudes. This highlights that atmosphere-only aquaplanet simulations with fixed freezing thresholds to realise ice-free conditions can alter extratropical dynamics, whereas allowing SSTs to fall below freezing yields a more physically consistent thermal structure and a more realistic storm-track response.

Results from these simple experiments demonstrate that the proposed framework enables controlled examination of the response of the atmospheric circulation, energy cycle,

and water cycle to changes in different frontal parameters. The flexibility with which these parameters can be modulated is a central advantage of the proposed setup relative to existing approaches based on prescribed observational SSTs (e.g., Nakamura et al., 2008; Ogawa et al., 2016; Ogawa and Spengler, 2024), in which the atmospheric response reflects the combined influence of multiple co-varying features in the observed SST field. The framework also complements idealised aquaplanet experiments that employ smoothly varying or zonally symmetric SST distributions (e.g., Neale and Hoskins, 2000; Brayshaw et al., 2008; Blackburn et al., 2013; Williamson et al., 2013; Schemm and Röthlisberger, 2024). Those experiments provide a valuable means of investigating the large-scale response to SST forcing, but do not explicitly represent a localised SST front. By prescribing the location, strength, width, and sharpness of the SST front independently, our approach allows to causally isolate the atmospheric response to distinct frontal characteristics. At the same time, the midlatitude SST front can be removed or weakened, allowing the framework to recover the broader class of smooth SST distributions commonly used in aquaplanet experiments.

The ability to independently control key geometric properties of midlatitude SST fronts as introduced in this study makes the framework well suited to future investigations of surface-forcing and thermodynamic influences on storm-track variability. Its flexibility also enables several natural extensions. For example, shifting the SST gradient profile latitudinally can represent non-equinox conditions and thereby facilitate investigation of seasonal effects, such as differences between the summer and winter hemispheres. Zonal variations in the SST front can likewise be incorporated to emulate and assess the atmospheric response to frontal waviness (i.e., by varying F with longitude), or to changes in frontal width (i.e., varying D and/or G) which are commonly associated with western boundary currents. Finally, allowing the frontal parameters to vary in time would also make it possible to represent a meandering SST front. Such extensions would allow for a systematic assessment of how zonally asymmetric SST structures influence storm-track dynamics, the hydrological cycle, and the global energy budget.

Appendix A: Analytical details of SST profile

The analytical expression for the SST profile is obtained by integrating Eq. (1) piecewise,

$$\mathrm{SST}(\varphi) = \mathrm{SST}_{\max} + \begin{cases} -\frac{1}{2}\alpha\varphi^2 & |\varphi| \le \phi_{\mathrm{T}} \\ +\frac{1}{2}\beta\phi_{\mathrm{T}} - \beta|\varphi| & \phi_{\mathrm{T}} < |\varphi| \le \phi_E \\ +\frac{1}{2}\beta\phi_{\mathrm{T}} - \frac{1}{2}\gamma\phi_E^2 + (\gamma\phi_E - \beta)|\varphi| - \frac{1}{2}\gamma\varphi^2 & \phi_E < |\varphi| \le \phi_{\mathrm{F}} \\ +\frac{1}{2}\beta\phi_{\mathrm{T}} - \frac{1}{2}\gamma(\Delta\phi_{\mathrm{F}}^2 - 2\phi_{\mathrm{F}}\phi_P) - (\beta + \gamma\phi_P)|\varphi| + \frac{1}{2}\gamma\varphi^2 & \phi_{\mathrm{F}} < |\varphi| \le \phi_P \\ +\frac{1}{2}\beta\phi_{\mathrm{T}} - \gamma\Delta\phi_{\mathrm{F}}^2 - \beta|\varphi| & \phi_P < |\varphi| \le \phi_0 \\ +\frac{1}{2}\beta\phi_{\mathrm{T}} - \gamma\Delta\phi_{\mathrm{F}}^2 - \beta\phi_0 & \phi_0 < |\varphi| \le 90^\circ \end{cases}. \quad \text{(A1)}$$

From Eq. (A1), we find the analytical expression for the latitude of the freezing edge,

$$\phi_0 = \frac{1}{2}\phi_{\mathrm{T}} + \frac{1}{\beta}\Delta\mathrm{SST} - \frac{1}{\beta}\Delta\phi_{\mathrm{F}}|\nabla\mathrm{SST}|_{\max}, \quad \text{(A2)}$$

where $\Delta\mathrm{SST} = \mathrm{SST}_{\max} - \mathrm{SST}_{\min}$. The freezing latitude ϕ_0 thus only depends on the intensity and width of the front but not on its position (no ϕ_{F} in Eq. A2).

Appendix B: Sensitivity to model resolution

We assess the sensitivity of our results to model resolution by running the control (F45) and no-front (NF) experiments at higher horizontal resolutions, specifically at T159 (0.75° at the Equator) and T239 (0.5° at the Equator). The impact of increasing horizontal resolution on the subtropical and midlatitude jets is marginal, with virtually no changes in both their spatial structure and intensity (Fig. B1a, b). The largest effects are found in the meridional wind variance (Fig. B1c, d), which is slightly stronger poleward of the SST front in T159 and T239 compared to T79 for both F45 and NF, though the overall structure does not change as the maximum $[v'v']$ does not shift in latitude. Changes in meridional heat transport $[v'T']$ (Fig. B1e, f) are also marginal and the response of the water cycle is nearly identical across the three resolutions (Fig. B1g, h). Overall, results indicate that horizontal resolution does not play a key role, at least for resolutions of T239 and below.

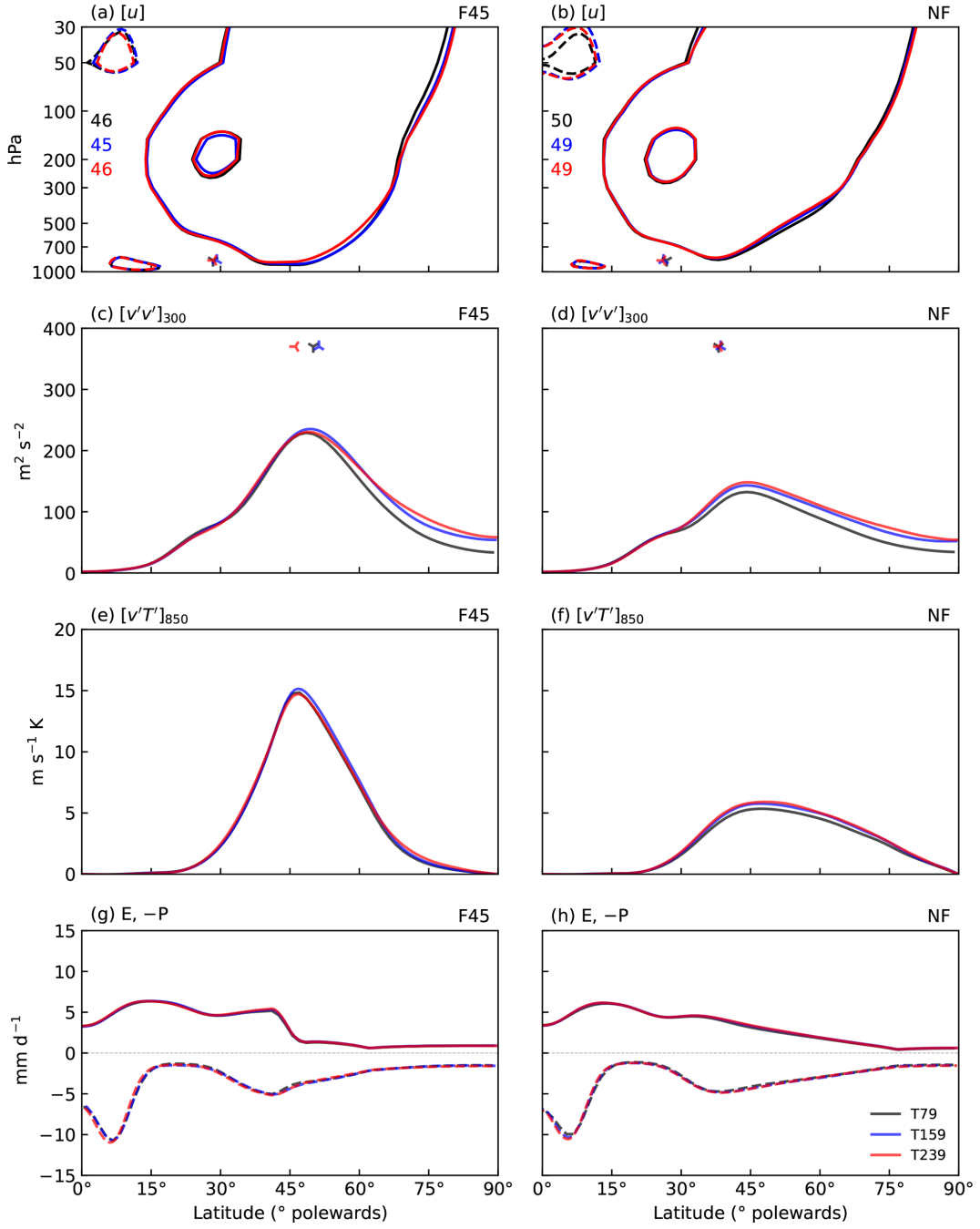


Figure B1. Climatological zonal means based on F45 **(a, c, e, g)** and NF **(b, d, f, h)** with horizontal resolution at T79 (black), T159 (blue), and T239 (red). **(a, b)** Zonal wind u (contours at -10, 10, 40 m s^{-1}, negative dashed), with maximum value within subtropical jet noted accordingly; markers indicate the latitude of reversal of the zonal wind at the surface (specific orientation bears no meaning). **(c, d)** $[v'v']$ at 300 hPa; markers indicate the latitude of maximum momentum flux divergence at 200 hPa. **(e, f)** $[v'T']$ at 850 hPa. **(g, h)** Zonally-averaged evaporation (E, solid) and precipitation (P, dashed, multiplied by -1).

Code and data availability. The specific version of AFES used to produce the results in this paper is archived on Zenodo at https://doi.org/10.5281/zenodo.19550344 (Ogawa and Marcheggiani, 2026), including input data and scripts to run the model.

Author contributions. FO, AM, and TS designed the numerical experiments. FO led the numerical simulations and analyses and contributed to finalising the manuscript. AM contributed to the analyses and led the manuscript writing. TS and HN led the scientific discussions, supervised the study, and contributed to finalising the manuscript.

Competing interests. The contact author has declared that none of the authors has any competing interests.

Disclaimer. Publisher's note: Copernicus Publications remains neutral with regard to jurisdictional claims made in the text, published maps, institutional affiliations, or any other geographical representation in this paper. The authors bear the ultimate responsibility for providing appropriate place names. Views expressed in the text are those of the authors and do not necessarily reflect the views of the publisher.

Acknowledgements. We thank Akira Kuwano-Yoshida and one anonymous reviewer for their helpful comments and suggestions, which helped improve the manuscript. Computing resources were provided by the Japan Agency for Marine-Earth Science and Technology (JAMSTEC).

Financial support. FO was supported by MEXT through the Grant-in-Aid for Transformative Research Areas (A) (grant no. 24H02229) and the Grant-in-Aid for Scientific Research (A) (grant no. 25H00687), as well as by the Arctic Challenge for Sustainability III (ArCS III; grant no. JPMXD1720251001) and SENTAN (grant no. JPMXD0722680395). FO and HN were additionally supported by the Ministry of the Environment of Japan through the Environment Research and Technology Development Fund (grant no. JPMEERF20242001). HN further acknowledges funding from the Japan Science and Technology Agency through the "ClimCORE" project (grant no. JPMJPF2013). AM and TS acknowledge funding from the Research Council of Norway (Norges Forskningsråd, NFR) through the BALMCAST project (NFR grant no. 324081).

Review statement. This paper was edited by Tilo Ziehn and reviewed by Akira Kuwano-Yoshida and one anonymous referee.

References

Blackburn, M. and Hoskins, B. J.: Context and aims of the Aqua-Planet Experiment, J. Meteorol. Soc. Jpn., 91, 1–15, https://doi.org/10.2151/jmsj.2013-A01, 2013.

Blackburn, M., Williamson, D. L., Nakajima, K., Ohfuchi, W., Takahashi, Y. O., Hayashi, Y.-Y., Nakamura, H., Ishiwatari, M., McGregor, J. L., Borth, H., Wirth, V., Frank, H., Bechtold, P., Wedi, N. P., Tomita, H., Satoh, M., Zhao, M., Held, I. M., Suarez, M. J., Lee, M.-I., Watanabe, M., Kimoto, M., Liu, Y., Wang, Z., Molod, A., Rajendran, K., Kitoh, A., and Stratton, R.: The Aqua-Planet Experiment (APE): CONTROL SST Simulation, J. Meteorol. Soc. Jpn., 91A, 17–56, https://doi.org/10.2151/jmsj.2013-A02, 2013.

Bluestein, H. B.: Observations and Theory of Weather Systems, Vol. 2: Synoptic-Dynamic Meteorology in Midlatitudes, Oxford University Press, New York, ISBN 9780195062687, https://global.oup.com/academic/product/synoptic-dynamic-meteorology-in-midlatitudes-9780195062687?cc=de&lang=en& (last access: 17 November 2026), 1993.

Booth, J. F., Thompson, L., Patoux, J., and Kelly, K. A.: Sensitivity of midlatitude storm intensification to perturbations in the sea surface temperature near the Gulf Stream, Mon. Weather Rev., 140, 1241–1256, https://doi.org/10.1175/MWR-D-11-00195.1, 2012.

Brachet, S., Codron, F., Feliks, Y., Ghil, M., Le Treut, H., and Simonnet, E.: Atmospheric circulations induced by a midlatitude SST front: A GCM study, J. Climate, 25, 1847–1853, https://doi.org/10.1175/JCLI-D-11-00329.1, 2012.

Brayshaw, D. J., Hoskins, B., and Blackburn, M.: The storm-track response to idealized SST perturbations in an aquaplanet GCM, J. Atmos. Sci., 65, 2842–2860, https://doi.org/10.1175/2008JAS2657.1, 2008.

Brayshaw, D. J., Hoskins, B., and Blackburn, M.: The basic ingredients of the North Atlantic storm track. Part I: Land–sea contrast and orography, J. Atmos. Sci., 66, 2539–2558, https://doi.org/10.1175/2009JAS3078.1, 2009.

Brayshaw, D. J., Hoskins, B., and Blackburn, M.: The basic ingredients of the North Atlantic storm track. Part II: Sea surface temperatures, J. Atmos. Sci., 68, 1784–1805, https://doi.org/10.1175/2011JAS3674.1, 2011.

Bui, H. and Spengler, T.: On the influence of sea surface temperature distributions on the development of extratropical cyclones, J. Atmos. Sci., 78, 1173–1188, https://doi.org/10.1175/JAS-D-20-0137.1, 2021.

Emanuel, K. A.: A scheme for representing cumulus convection in large-scale models, J. Atmos. Sci., 48, 2313–2329, https://doi.org/10.1175/1520-0469(1991)048<2313:ASFRCC>2.0.CO;2, 1991.

Enomoto, T., Kuwano-Yoshida, A., Komori, N., and Ohfuchi, W.: Description of AFES 2: Improvements for high-resolution and coupled simulations, in: High resolution numerical modelling of the atmosphere and ocean, Springer, 77–97, https://doi.org/10.1007/978-0-387-49791-4_5, 2008.

Graff, L. S. and LaCasce, J.: Changes in the extratropical storm tracks in response to changes in SST in an AGCM, J. Climate, 25, 1854–1870, https://doi.org/10.1175/JCLI-D-11-00174.1, 2012.

Grise, K. M. and Davis, S. M.: Hadley cell expansion in CMIP6 models, Atmos. Chem. Phys., 20, 5249–5268, https://doi.org/10.5194/acp-20-5249-2020, 2020.

Haualand, K. F. and Spengler, T.: Direct and indirect effects of surface fluxes on moist baroclinic development in an idealized framework, J. Atmos. Sci., 77, 3211–3225, https://doi.org/10.1175/JAS-D-19-0328.1, 2020.

Hersbach, H., Bell, B., Berrisford, P., Hirahara, S., Horányi, A., Muñoz-Sabater, J., Nicolas, J., Peubey, C., Radu, R., Schepers, D., Simmons, A., Soci, C., Abdalla, S., Abellan, X., Balsamo, G., Bechtold, P., Biavati, G., Bidlot, J., Bonavita, M., De Chiara, G., Dahlgren, P., Dee, D., Diamantakis, M., Dragani, R., Flemming, J., Forbes, R., Fuentes, M., Geer, A., Haimberger, L., Healy, S., Hogan, R. J., Hólm, E., Janisková, M., Keeley, S., Laloy-aux, P., Lopez, P., Lupu, C., Radnoti, G., de Rosnay, P., Rozum, I., Vamborg, F., Villaume, S., and Thépaut, J.-N.: The ERA5 global reanalysis, Q. J. Roy. Meteor. Soc., 146, 1999–2049, https://doi.org/10.1002/qj.3803, 2020.

Hirata, H., Kawamura, R., Kato, M., and Shinoda, T.: Response of rapidly developing extratropical cyclones to sea surface temperature variations over the western Kuroshio–Oyashio confluence region, J. Geophys. Res.-Atmos., 121, 3843–3858, https://doi.org/10.1002/2015JD024391, 2016.

Hotta, D. and Nakamura, H.: On the significance of the sensible heat supply from the ocean in the maintenance of the mean baroclinicity along storm tracks, J. Climate, 24, 3377–3401, https://doi.org/10.1175/2010JCLI3910.1, 2011.

Kosaka, Y., Kobayashi, S., Harada, Y., Kobayashi, C., Naoe, H., Yoshimoto, K., Harada, M., Goto, N., Chiba, J., Miyaoka, K., Sekiguchi, R., Deushi, M., Kamahori, H., Nakaegawa, T., Tanaka, T. Y., Tokuhiro, T., Sato, Y., Matsushita, Y., and Onogi, K.: The JRA-3Q reanalysis, J. Meteorol. Soc. Jpn., 102, 49–109, https://doi.org/10.2151/jmsj.2024-004, 2024.

Kuwano-Yoshida, A. and Minobe, S.: Storm-track response to SST fronts in the northwestern Pacific region in an AGCM, J. Climate, 30, 1081–1102, https://doi.org/10.1175/JCLI-D-16-0331.1, 2017.

Kuwano-Yoshida, A., Enomoto, T., and Ohfuchi, W.: An improved PDF cloud scheme for climate simulations, Q. J. Roy. Meteor. Soc.y, 136, 1583–1597, https://doi.org/10.1002/qj.660, 2010.

Louis, J.-F.: A parametric model of vertical eddy fluxes in the atmosphere, Bound.-Lay. Meteorol., 17, 187–202, https://doi.org/10.1007/BF00117978, 1979.

Lu, J., Chen, G., and Frierson, D. M.: The position of the midlatitude storm track and eddy-driven westerlies in aquaplanet AGCMs, J. Atmos. Sci., 67, 3984–4000, https://doi.org/10.1175/2010JAS3477.1, 2010.

Ma, X., Chang, P., Saravanan, R., Montuoro, R., Nakamura, H., Wu, D., Lin, X., and Wu, L.: Importance of resolving Kuroshio front and eddy influence in simulating the North Pacific storm track, J. Climate, 30, 1861–1880, https://doi.org/10.1175/JCLI-D-16-0154.1, 2017.

Marcheggiani, A. and Ambaum, M. H. P.: The role of heat-flux–temperature covariance in the evolution of weather systems, Weather Clim. Dynam., 1, 701–713, https://doi.org/10.5194/wcd-1-701-2020, 2020.

Marcheggiani, A. and Spengler, T.: Diabatic effects on the evolution of storm tracks, Weather Clim. Dynam., 4, 927–942, https://doi.org/10.5194/wcd-4-927-2023, 2023.

Marcheggiani, A. and Spengler, T.: Cold air outbreaks drive near-surface baroclinicity variability over storm track entrance regions in the Northern Hemisphere, Weather Clim. Dynam., 6, 1479–1489, https://doi.org/10.5194/wcd-6-1479-2025, 2025.

Marcheggiani, A., Dacre, H., Spensberger, C., and Spengler, T.: Weather features drive free-tropospheric baroclinicity variability in the North Atlantic storm track, Q. J. Roy. Meteor. Soc., 151, e5061, https://doi.org/10.1002/qj.5061, 2025.

Mellor, G. L. and Yamada, T.: Development of a turbulence closure model for geophysical fluid problems, Rev. Geophys., 20, 851–875, https://doi.org/10.1029/RG020i004p00851, 1982.

Michel, C. and Rivière, G.: Sensitivity of the position and variability of the eddy-driven jet to different SST profiles in an aquaplanet general circulation model, J. Atmos. Sci., 71, 349–371, https://doi.org/10.1175/JAS-D-13-074.1, 2014.

Nakajima, T. and Tanaka, M.: Matrix formulations for the transfer of solar radiation in a plane-parallel scattering atmosphere, J. Quant. Spectrosc. Ra., 35, 13–21, https://doi.org/10.1016/0022-4073(86)90088-9, 1986.

Nakamura, H. and Shimpo, A.: Seasonal Variations in the Southern Hemisphere Storm Tracks and Jet Streams as Revealed in a Reanalysis Dataset, J. Climate, 17, 1828–1844, https://doi.org/10.1175/1520-0442(2004)017<1828:SVITSH>2.0.CO;2, 2004.

Nakamura, H., Sampe, T., Tanimoto, Y., and Shimpo, A.: Observed associations among storm tracks, jet streams and midlatitude oceanic fronts, Earth's Climate: The Ocean–Atmosphere Interaction, Geophys. Monogr., 147, 329–345, https://doi.org/10.1029/147GM18, 2004.

Nakamura, H., Sampe, T., Goto, A., Ohfuchi, W., and Xie, S.-P.: On the importance of midlatitude oceanic frontal zones for the mean state and dominant variability in the tropospheric circulation, Geophys. Res. Lett. 35, L15709, https://doi.org/10.1029/2008GL034010, 2008.

Neale, R. B. and Hoskins, B. J.: A standard test for AGCMs including their physical parametrizations: I: The proposal, Atmos. Sci. Lett., 1, 101–107, https://doi.org/10.1006/asle.2000.0019, 2000.

Nonaka, M., Nakamura, H., Taguchi, B., Komori, N., Kuwano-Yoshida, A., and Takaya, K.: Air–sea heat exchanges characteristic of a prominent midlatitude oceanic front in the South Indian Ocean as simulated in a high-resolution coupled GCM, J. Climate, 22, 6515–6535, https://doi.org/10.1175/2009JCLI2960.1, 2009.

Ogawa, F. and Marcheggiani, A.: Model, input data, and run scripts for "Idealised framework to prescribe sea surface temperatures to investigate the atmospheric circulation response", Zenodo [code and data set], https://doi.org/10.5281/zenodo.19550344, 2026.

Ogawa, F. and Spengler, T.: Prevailing surface wind direction during air–sea heat exchange, J. Climate, 32, 5601–5617, https://doi.org/10.1175/JCLI-D-18-0752.1, 2019.

Ogawa, F. and Spengler, T.: Influence of mid-latitude sea surface temperature fronts on the atmospheric water cycle and storm track activity, Weather Clim. Dynam., 5, 1031–1042, https://doi.org/10.5194/wcd-5-1031-2024, 2024.

Ogawa, F., Nakamura, H., Nishii, K., Miyasaka, T., and Kuwano-Yoshida, A.: Dependence of the climatological axial latitudes of the tropospheric westerlies and storm tracks on the latitude of an extratropical oceanic front, Geophys. Res. Lett., 39, https://doi.org/10.1029/2011GL049922, 2012.

Ogawa, F., Omrani, N.-E., Nishii, K., Nakamura, H., and Keenlyside, N.: Ozone-induced climate change propped up by the Southern Hemisphere oceanic front, Geophys. Res. Lett., 42, 10056–10063, https://doi.org/10.1002/2015GL066538, 2015.

Ogawa, F., Nakamura, H., Nishii, K., Miyasaka, T., and Kuwano-Yoshida, A.: Importance of midlatitude oceanic frontal zones

for the annular mode variability: Interbasin differences in the southern annular mode signature, J. Climate, 29, 6179–6199, https://doi.org/10.1175/JCLI-D-15-0885.1, 2016.

Ohfuchi, W., Nakamura, H., Yoshioka, M., Enomoto, T., Takaya, K., Peng, X., Yamane, S., Nishimura, T., Kurihara, Y., and Ninomiya, K.: 10-km mesh meso-scale resolving simulations of the global atmosphere on the Earth Simulator: Preliminary outcomes of AFES (AGCM for the Earth Simulator), J. Earth Simulator, 1, 8–34, https://doi.org/10.32131/jes.1.8, 2004.

Okajima, S., Nakamura, H., and Spengler, T.: Midlatitude oceanic fronts strengthen the hydrological cycle between cyclones and anticyclones, Geophys. Res. Lett., 51, e2023GL106187, https://doi.org/10.1029/2023GL106187, 2024.

O'Reilly, C. H., Minobe, S., Kuwano-Yoshida, A., and Woollings, T.: The Gulf Stream influence on wintertime North Atlantic jet variability, Q. J. Roy. Meteor. Soc., 143, 173–183, https://doi.org/10.1002/qj.2907, 2017.

O'Reilly, C. H., Minobe, S., and Kuwano-Yoshida, A.: The influence of the Gulf Stream on wintertime European blocking, Clim. Dynam., 47, 1545–1567, https://doi.org/10.1007/s00382-015-2919-0, 2016.

Papritz, L. and Spengler, T.: Analysis of the slope of isentropic surfaces and its tendencies over the North Atlantic, Q. J. Roy. Meteor. Soc., 141, 3226–3238, https://doi.org/10.1002/qj.2605, 2015.

Parfitt, R., Czaja, A., Minobe, S., and Kuwano-Yoshida, A.: The atmospheric frontal response to SST perturbations in the Gulf Stream region, Geophys. Res. Lett., 43, 2299–2306, https://doi.org/10.1002/2016GL067723, 2016.

Piazza, M., Terray, L., Boé, J., Maisonnave, E., and Sanchez-Gomez, E.: Influence of small-scale North Atlantic sea surface temperature patterns on the marine boundary layer and free troposphere: A study using the atmospheric ARPEGE model, Clim. Dynam., 46, 1699–1717, https://doi.org/10.1007/s00382-015-2669-z, 2016.

Sampe, T., Nakamura, H., Goto, A., and Ohfuchi, W.: Significance of a midlatitude SST frontal zone in the formation of a storm track and an eddy-driven westerly jet, J. Climate, 23, 1793–1814, https://doi.org/10.1175/2009JCLI3163.1, 2010.

Schemm, S. and Röthlisberger, M.: Aquaplanet simulations with winter and summer hemispheres: model setup and circulation response to warming, Weather Clim. Dynam., 5, 43–63, https://doi.org/10.5194/wcd-5-43-2024, 2024.

Seo, H., O'Neill, L. W., Bourassa, M. A., Czaja, A., Drushka, K., Edson, J. B., Fox-Kemper, B., Frenger, I., Gille, S. T., Kirtman, B. P., Minobe, S., Pendergrass, A. G., Renault, L., Roberts, M. J., Schneider, N., Small, R. J., Stoffelen, A., and Wang, Q.: Ocean Mesoscale and Frontal-Scale Ocean–Atmosphere Interactions and Influence on Large-Scale Climate: A Review, J. Climate, 36, 1981–2013, https://doi.org/10.1175/JCLI-D-21-0982.1, 2023.

Small, R. J., Tomas, R. A., and Bryan, F. O.: Storm track response to ocean fronts in a global high-resolution climate model, Clim. Dynam., 43, 805–828, https://doi.org/10.1007/s00382-013-1980-9, 2014.

Taguchi, B., Nakamura, H., Nonaka, M., and Xie, S.-P.: Influences of the Kuroshio/Oyashio Extensions on air–sea heat exchanges and storm-track activity as revealed in regional atmospheric model simulations for the 2003/04 cold season, J. Climate, 22, 6536–6560, https://doi.org/10.1175/2009JCLI2910.1, 2009.

Tsopouridis, L., Spengler, T., and Spensberger, C.: Smoother versus sharper Gulf Stream and Kuroshio sea surface temperature fronts: effects on cyclones and climatology, Weather Clim. Dynam., 2, 953–970, https://doi.org/10.5194/wcd-2-953-2021, 2021a.

Tsopouridis, L., Spensberger, C., and Spengler, T.: Characteristics of cyclones following different pathways in the Gulf Stream region, Q. J. Roy. Meteor. Soc., 147, 392–407, https://doi.org/10.1002/qj.3924, 2021b.

Tsopouridis, L., Spensberger, C., and Spengler, T.: Cyclone intensification in the Kuroshio region and its relation to the sea surface temperature front and upper-level forcing, Q. J. Roy. Meteor. Soc., 147, 485–500, https://doi.org/10.1002/qj.3929, 2021c.

Uno, I., Cai, X.-M., Steyn, D. G., and Emori, S.: A simple extension of the Louis method for rough surface layer modelling, Bound.-Lay. Meteor., 76, 395–409, https://doi.org/10.1007/BF00709241, 1995.

Weijenborg, C. and Spengler, T.: Diabatic heating as a pathway for cyclone clustering encompassing the extreme storm Dagmar, Geophys. Res. Lett., 47, e2019GL085777, https://doi.org/10.1029/2019GL085777, 2020.

Williamson, D. L., Blackburn, M., Nakajima, K., Ohfuchi, W., Takahashi, Y. O., Hayashi, Y.-Y., Nakamura, H., Ishiwatari, M., McGregor, J. L., Borth, H., Wirth, V., Frank, H., Bechtold, P., Wedi, N. P., Tomita, H., Satoh, M., Zhao, M., Held, I. M., Suarez, M. J., Lee, M.-I., Watanabe, M., Kimoto, M., Liu, Y., Wang, Z., Molod, A., Rajendran, K., Kitoh, A., and Stratton, R.: The Aqua-Planet Experiment (APE): Response to changed meridional SST profile, J. Meteorol. Soc. Jpn., 91A, 57–89, https://doi.org/10.2151/jmsj.2013-A03, 2013.

Yao, Y., Zhong, Z., and Yang, X.-Q.: Numerical experiments of the storm track sensitivity to oceanic frontal strength within the Kuroshio/Oyashio Extensions, J. Geophys. Res.-Atmos., 121, 2888–2900, https://doi.org/10.1002/2015JD024381, 2016.